catalysts

MDPI

Article

A Comparative Discussion of the Catalytic Activity and CO_2-Selectivity of Cu-Zr and Pd-Zr (Intermetallic) Compounds in Methanol Steam Reforming

Norbert Köpfle [1], Lukas Mayr [1], Daniela Schmidmair [2], Johannes Bernardi [3], Axel Knop-Gericke [4], Michael Hävecker [4], Bernhard Klötzer [1] and Simon Penner [1,*]

1 Institute of Physical Chemistry, University of Innsbruck, Innrain 80-82, A-6020 Innsbruck, Austria; norbert.koepfle@uibk.ac.at (N.K.); l.mayr@uibk.ac.at (L.M.); bernhard.kloetzer@uibk.ac.at (B.K.)

2 Institute of Mineralogy and Petrography, University of Innsbruck, Innrain 52d, A-6020 Innsbruck, Austria; daniela.schmidmair@uibk.ac.at

3 University Service Facility for Transmission Electron Microscopy (USTEM), Technische Universität Wien, Wiedner Hauptstrasse 8-10/057B, A-1040 Wien, Österreich; johannes.bernardi@tuwien.ac.at

4 Department of Inorganic Chemistry, Fritz-Haber-Institute of the Max-Planck-Society, Faradayweg 4-6, D-14195 Berlin, Germany; knop@fhi-berlin.mpg.de (A.K.-G.); michael.haevecker@helmholtz-berlin.de (M.H.)

* Correspondence: simon.penner@uibk.ac.at; Tel.: +43-512-507-58003

Academic Editor: Benoît Louis

Received: 10 January 2017; Accepted: 7 February 2017; Published: 9 February 2017

Abstract: The activation and catalytic performance of two representative Zr-containing intermetallic systems, namely Cu-Zr and Pd-Zr, have been comparatively studied operando using methanol steam reforming (MSR) as test reaction. Using an inverse surface science and bulk model catalyst approach, we monitored the transition of the initial metal/intermetallic compound structures into the eventual active and CO_2-selective states upon contact to the methanol steam reforming mixture. For Cu-Zr, selected nominal stoichiometries ranging from Cu:Zr = 9:2 over 2:1 to 1:2 have been prepared by mixing the respective amounts of metallic Cu and Zr to yield different Cu-Zr bulk phases as initial catalyst structures. In addition, the methanol steam reforming performance of two Pd-Zr systems, that is, a bulk system with a nominal Pd:Zr = 2:1 stoichiometry and an inverse model system consisting of CVD-grown ZrO_xH_y layers on a polycrystalline Pd foil, has been comparatively assessed. While the CO_2-selectivity and the overall catalytic performance of the Cu-Zr system is promising due to operando formation of a catalytically beneficial Cu-ZrO_2 interface, the case for Pd-Zr is different. For both Pd-Zr systems, the low-temperature coking tendency, the high water-activation temperature and the CO_2-selectivity spoiling inverse WGS reaction limit the use of the Pd-Zr systems for selective MSR applications, although alloying of Pd with Zr opens water activation channels to increase the CO_2 selectivity.

Keywords: Zirconium-*tert.*-butoxide; Palladium; Zr reduction; methanol steam reforming; copper

1. Introduction

ZrO_2-containing catalysts have evoked recent interest both as additives to other catalytic systems and as isolated entities as well as for their ability to improve the structural integrity of various catalysts and to induce beneficial steering of reaction pathways to increase the respective selectivity of especially the methanol steam reforming (MSR) and methanol synthesis reactions [1–6]. Particularly rewarding in this respect is to focus on the Cu-ZrO_2 system, where the addition of ZrO_2 to the industrially

used $Cu/ZnO/Al_2O_3$ catalyst has already been shown to increase the long-term stability of the system and to prevent the Cu particles from extensive sintering. Improved catalytic performance, involving direct Cu-ZrO_2 interaction and the eventual formation of Cu–O–Zr bonds, have also been reported for clean Cu-ZrO_2 catalysts. It is widely accepted that the structure and chemistry of the metal-oxide Cu-ZrO_2 phase boundary is most crucial for developing beneficial catalytic properties [7–13]. For methanol steam reforming, the key parameters are high CO_2 selectivity, maximum hydrogen yield and a low CO concentration in the product feed [4]. The opening of proper water activation channels is thereby an obvious prerequisite for CO_2-selective steam reforming. As such, it has been shown recently for differently prepared Cu-ZrO_2 model systems, that the reversible hydroxylation capability of ZrO_2 (yielding ZrO_xH_y species) at the interface is a prime criterion for efficient water activation [14–16]. In due course, the latter can be achieved best by in situ self activation of a Cu-Zr bimetallic compound, which, upon contact with the steam reforming mixture at 623 K, is decomposed into a "supported" Cu-ZrO_2 catalyst comprised of small dispersed metallic Cu particles in intimate contact with partially hydroxylated ZrO_2 crystallizing predominantly in the tetragonal modification. This synergistically self-activated catalyst shows the most promising CO_2 selectivity at close to 100% [15]. Extending this concept to other promising methanol steam reforming catalysts on bimetallic compound "precatalyst" basis suggests focusing on a group of CO_2-selective Pd-based intermetallic compounds studied exhaustively in the last two decades [17]. Foremost, this includes the Zn-Pd, Ga-Pd and In-Pd systems, on which the importance of water activation by creation of bifunctionally operating ZnO-ZnPd/Ga_2O_3-$GaPd_2$/In_2O_3-InPd interfaces (for simultaneous methanol and water activation) during methanol steam reforming has been clearly worked out [18]. The interpretation of the catalytic behavior of these types of intermetallic phases was given in terms of a similar electronic structure of the Pd-based intermetallic phases and metallic Cu, which has been proven experimentally and theoretically [18]. Similar ideas also hold for the catalytic properties of the intermetallic compounds/near-surface alloys of Cu-Zn and Cu-Zr [19]. It is therefore clear that the beneficial catalytic function of Zn/ZnO can be at least to some extent be modeled by Zr/ZrO_2. Transferring these ideas to preparing a potentially catalytically active Pd-ZrO_2 interface by proper adjustment of the synthesis conditions of a Pd-Zr(O_2) model system yielded two important results: (i) redox-active metallic Zr sub-nanometer clusters via reduction of a partially hydroxylated Zr^{4+}-containing layer obtained following adsorption and thermal annealing of the organometallic precursor material Zr-*tert.* Butoxide; and (ii) the promotion of methane dry reforming if initially metallic Zr species are present in the precursor, which subsequently lead to a Pd/ZrH_xO_y phase boundary by oxidative activation under operando conditions. A comparable methane dry reforming (DRM) behavior has also been found for a bulk Pd-Zr intermetallic phase with deliberately chosen Pd:Zr = 2:1 nominal stoichiometry (in close correlation to the Cu-Zr bulk system discussed above) [20]. Under methanol steam reforming conditions, preliminary results indicate the principal water activation capability of the Pd-ZrO_2 interface, albeit with so far unsatisfactory CO_2 selectivity. In order to work out the structural and catalytic similarities and differences between the Cu-Zr and the Pd-Zr system, we here aim to provide a direct comparison of the behavior of the respective Cu-Zr and Pd-Zr bulk bimetallic catalyst entities in methanol steam reforming. Particular emphasis will be given to the elucidation of an eventual similar structural and chemical self-activation on Pd-Zr and to the behavior of the so far only DRM-tested active Pd/ZrH_xO_y phase boundary in methanol steam reforming.

2. Results and Discussion

2.1. Inverse Pd/ZrO_xH_y Samples and Pd-Zr Intermetallic Compounds

Catalytic, structural and spectroscopic characterization has been carried out on the two selected Pd-Zr systems discussed in detail in the Methods and Materials Section. As such, an inverse model system of ZrO_xH_y overlayers on Pd resulting from thermal decomposition of 1000 L Zirconium-*tert.* butoxide (ZTB) at 693 K and a bulk intermetallic Pd-Zr system have been comparatively included in

the discussion. In a previous report, we have already addressed the CVD preparation of the layers and the susceptibility of the Zr oxidation state to the chemical environment—especially under reducing conditions [19].

2.1.1. Methanol Steam Reforming on the Inverse Pd/ZrO_xH_y Sample

In due course, the CVD "as-prepared" (1000 L ZTB at 693 K, resulting in ~0.5 monolayers (ML) ZrO_xH_y) and a partially reduced sample (annealed to 700 K in 5×10^{-9} mbar vacuum after CVD) were tested in the batch reactor setup for MSR. In our standard temperature-programmed experiment up to 673 K, in both cases no positive synergistic effects toward enhanced CO_2 selectivity were observed. The well-known methanol dehydrogenation activity of clean Pd toward almost 100% CO and H_2 was found to scale linearly with the fraction of ZrO_xH_y-free Pd surface. However, water-activating and, thus, CO_2-promoting phase boundary effects could be verified under otherwise identical MSR conditions for related inverse Cu/ZrO_2 and Cu/ZrO_xH_y model catalysts [14–16]. Even the "hydroxylative" activation of Zr^0 on the vacuum-pre-reduced $Pd/Zr^0/Zr^{+4}O_xH_y$ catalyst surface under MSR conditions does not promote low-temperature ($T < 623$ K) water activation and, thus, direct CO_2-formation, which so far could be verified for the related bimetallic PdZn [18], CuZn [19] and CuZr [15] surfaces. Even for the later discussed intermetallic Pd-Zr bulk phase, no increase in the CO_2 formation rate could be found in MSR in similar temperature regimes.

From the electronic structure viewpoint, full dehydrogenation of methanol via formaldehyde to CO occurs at a high rate only on the "clean" (electronically unaltered) Pd metal surface, since formaldehyde is clearly destabilized on Pd^0 [21], which moreover features intrinsically poor water activation properties. In contrast, both on clean Cu^0 and the ZnPd intermetallic (which are both MSR stable), full dehydrogenation toward CO is blocked [18,19]. If, in due course, the pathway for water activation and thus total oxidation of formaldehyde toward CO_2 is opened, high CO_2 selectivity can be realized. On the other hand, intermetallic precursors containing Zr^0 are in general unstable under MSR conditions, leading either to exsolution of clean metallic Cu^0 (with little dehydrogenation propensity for HCHO and also reduced coking propensity) or to surface-near formation of extended unalloyed Pd^0 patches. For the latter, fast full dehydrogenation is expected to be dominant over total oxidation of HCHO to CO_2, especially if the MSR-induced metal-zirconia phase boundary is inactive or somehow inactivated regarding water activation.

The latter aspect implies a further reason for the complete absence of any CO_2-beneficial Pd-Zr interaction, which was identified by in situ X-ray photoelectron (XPS) measurements. In Figure 1, the evolution of the Pd 3d, Zr 3d, C 1s and O 1s regions after sequential treatments under MSR conditions, in clean methanol, water atmosphere and in O_2, are shown, starting from the CVD as-grown Pd/ZrO_xH_y pre-catalyst state. In excess of water (water:methanol = 2:1), only very little carbon formation was observed at ~700 K (compare Figure 1, lowest panel vs. Figure 2 (different scale for C 1s)). As soon as water is switched off (giving rise to a clean methanol atmosphere), a carbon layer quickly starts to grow. This carbon is mostly assigned to graphitic species, according to the dominant C 1s binding energy (BE) component at 284.2 eV and the quite low full width at half maximum(FWHM) of the C 1s peak of ~0.5 eV. If the temperature is increased stepwise, the C 1s signal grows. Even though graphitic carbon is known for its rather less pronounced inelastic photoelectron attenuation effect (as it can be used as an electron transparent layer in the form of graphene [22]), the observed large amount of carbon (well above 1 ML) must in principle cause a certain shielding effect both for the Pd 3d and Zr 3d signals if it was homogeneously covering the entire surface, especially upon consideration of the highly surface-sensitive operation mode (photoelectron kinetic energy ~120 eV). Surprisingly, this expectable attenuation strongly affects the Pd 3d region, but the Zr 3d signal remains almost unchanged. This effect can in principle be explained in two ways: Either, (1) Graphite only grows on Pd, but not on ZrO_xH_y, creating a thick carbon overlayer with holes at the ZrO_2 islands. Pd-Zr interfacial sites do not get lost, but are blocked by graphitic carbon, resulting in the loss of any beneficial catalytic effect of these special sites. This hypothesis would also imply that the ZrO_2 islands are thick enough to

be fully Pd 3d "attenuating", otherwise a carbon coverage-independent Pd 3d signal passing through the ZrO_xH_y islands should remain detectable. With the used photon energy of 120 eV the island height would have to exceed at least 3 ML. Considering the scanning tunneling microscopic (STM) images (cf. Figure 4 in Ref. [19]), which show a ZrO_xH_y-carbon overlayer on Pd(111) with a coverage close to 1 ML after CVD, and evenly distributed clusters of Zr atoms with 1 ML height after the subsequent UHV annealing step, this scenario appears rather doubtful. Therefore, a second explanation might be more reasonable, but is only tentative at the moment: (2) Carbon grows in a "sandwich-like" fashion between Pd and ZrO_xH_y and "lifts" the ZrO_xH_y islands up. Consequently, the Pd-Zr interfacial sites would also get lost, resulting in the discussed catalytic inactivity. Note that such tremendous amounts of carbon were found neither on clean Pd nor on clean ZrO_2 under otherwise identical conditions. Therefore, a strong enhancement of coking caused by the Pd/ZrO_xH_y interface is strongly suggested. In such a way, the inactivity of the phase boundary in the water-containing MSR atmosphere might also be rationalized: The boundary-site-blocking or beginning lift off effect is expected to already play a role, even though the carbon formation propensity is lowered due to the simultaneous water co-feed. Smaller amounts of graphitic carbon (C 1s BE = 284.3 eV) were always observed ex situ after MSR in the batch reactor setup. Moreover, MSR in situ XPS experiments at temperatures lower than 700 K (Figure 2) clearly indicate the formation of graphitic carbon also under MSR conditions. Quantification indicates a carbon coverage of 0.5–1 ML at 700 K under MSR conditions and around 1.5 ML at 700 K under pure methanol. As the formed carbon "interlayer" caused by pure methanol between 700 K and 750 K cannot be removed with H_2O and not even with O_2 at 750 K, as shown in the uppermost panels of Figure 1, its permanent poisoning effect and ineffective removal by water under MSR conditions is obvious.

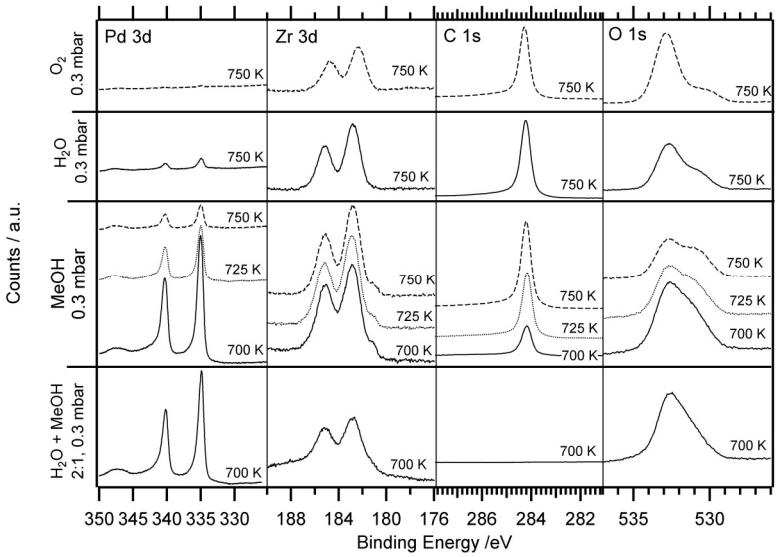

Figure 1. In situ near-ambient pressure X-ray photoelectron (NAP-XP) spectra (Pd 3d, Zr 3d, C 1s and O 1s (overlapping with Pd 3p) regions) of CVD-grown 0.5 ML ZrO_xH_y on a Pd model catalyst after 1000 L Zirconium *tert.* butoxide (ZTB) at 723 K under water-rich methanol steam reforming (MSR) conditions, in clean methanol, water and oxygen (details see left axis). No vacuum annealing treatment after chemical vapor deposition (CVD) was performed.

Starting from a partially reduced initial Zr state (CVD with ZTB followed by vacuum annealing [20]), Figure 2 shows the temperature-dependent evolution of the in situ XPS spectra under MSR conditions. Up to 423 K, carbon oxygenate species can be seen at binding energies around 286–288 eV. They arise from partial oxidation of methanol and prove the potential of the surface for methanol activation. Up to 548 K no Zr hydroxylation is found. With increasing temperature, hydroxylation takes place under reaction conditions, along with a shift of the Zr 3d peak from

182.3 up to 183.0 eV due to reaction with H_2O in the gas feed. This indicates water activation and suggests the opening of water activation-dependent reaction channels. Moreover, graphitic carbon species (BE of 284.2 eV) are increasing between 298 and 648 K under MSR conditions. These carbon species disappear at higher temperatures. Both carbon bulk dissolution in Pd and the water gas reaction $C + H_2O \rightarrow CO + H_2$, which can cause the onset of CO formation above 623 K (see Figure 3), may be considered to explain this observation. In the O 1s region, special care has to been taken when interpreting the peak shift to higher BE as Zr hydroxylation, since also carbon oxygenates may contribute to this trend and O 1s overlaps with Pd 3p.

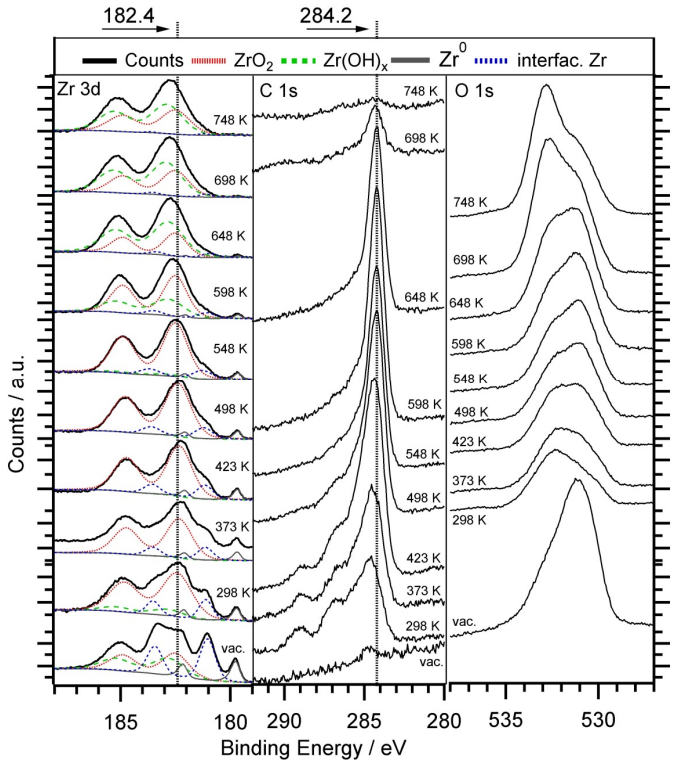

Figure 2. In situ NAP-XPS spectra (Zr 3d, C 1s and O 1s (overlapping with Pd 3p) regions) of 0.5 monolayers (ML) Zr^0/ZrO_xH_y, prepared by annealing of CVD grown ZrO_xH_y (2000 L ZTB at 723 K) in vacuum at 700 K under water-rich MSR conditions (H_2O:MeOH = 2:1, p_{total} = 0.3 mbar).

As mentioned above, neither the CVD-as-grown $Pd/Zr^{+4}O_xH_y$ nor the mixed valence $Pd/Zr^0/ZrO_xH_y$ model catalyst (prepared by vacuum annealing of the former) showed synergistic MSR effects in the standard temperature range up to 623 K. This range represents also the accumulation and stability region of surface/interface carbon species, as verified by the in situ XPS experiments of Figure 2. As the spectra at $T > 648$ K in Figure 2 both indicate additional surface hydroxylation by water and pronounced carbon clean-off, high-temperature MSR experiments up to 873 K were additionally performed and are shown in Figure 3. Formation of CO starts around 623 K and is assigned to the intrinsic methanol dehydrogenation activity of the residual clean Pd surface. On the initially clean Pd foil (without Zr), this reaction starts also slightly above 600 K. At ~700 K the CO formation rate passes through a maximum, then drops steeply and even becomes negative, i.e., already formed CO is consumed, which is clearly linked to simultaneous positive CO_2 formation. It is rather conclusive that the CO_2 formation arises from the onset of water gas shift (WGSR) activity, which is again coupled with the pronounced carbon clean-off effect starting above 650 K and shown in Figure 2. Thus, we suggest a water activation—carbon clean off—WGSR scenario mediated by "de-coked" and hence, activated Pd/ZrO_xH_y sites above ~650 K. The catalytic results of Figure 3 are therefore consistent with the in situ XP spectra of Figure 2. In the isothermal reaction part, CO is still formed on Pd, but partially

re-consumed by the water gas shift reaction to form CO_2. Consequently, both formation rates, CO and CO_2, are positive. On this basis, we have to conclude that the low-temperature coking tendency, the high water-activation temperature and the CO_2-forming WGS reaction on the "re-activated" catalyst limit the relevance of Pd/ZrO_xH_y for highly selective MSR applications, which are intrinsically impossible due to the temperature-dependent WGS equilibrium.

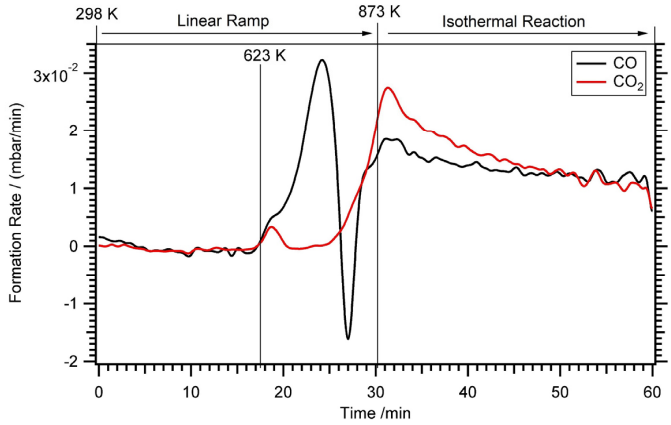

Figure 3. MSR on the CVD grown ZrO_xH_y model catalyst under water-rich MSR conditions (water:methanol = 2:1, p_{total} = 36 mbar). The exposure was about 1000 L ZTB at 700 K and the initial coverage with Zr estimated to ~0.4 ML. The temperature range of the MSR experiment was extended to 873 K.

2.1.2. Methanol Steam Reforming on the Pd-Zr Bulk Sample

To further test the ability of Pd-Zr systems to act as active and potentially CO_2-selective methanol steam reforming catalysts, and to connect also to recent experiments on the formation of a bifunctional synergistically operating Cu-ZrO_2 interface obtained by oxidative decomposition of Cu-Zr intermetallic phases with a nominal Cu:Zr = 2:1 stoichiometry [18], we prepared a similar Pd-Zr bulk intermetallic system. Preparation was carried out as discussed in the Methods and Materials Section. Of particular importance in this respect is the question, whether a single Pd-Zr intermetallic phase could be prepared that exhibits beneficial hydroxylation kinetics already at low enough temperatures, eventually enabling to access CO_2-selective MSR pathways.

Figure 4 shows a comparison of the XRD-derived bulk structures before and after the methanol steam reforming experiment up to 873 K. Before MSR, the XRD pattern can be consistently explained by the presence of a body-centered tetragonal Pd_2Zr phase [23] in co-existence with metallic Pd. Pd_3Zr [24] is additionally present as a minor component. Note that peaks of the underlying Ta substrate used for preparing the Pd-Zr intermetallic compound are visible, as the latter is not removed from the substrate for XRD analysis. The discussed findings are comparable to those of the 2:1 Cu-Zr system, where in essence also an admixture of metallic Cu and $Cu_{51}Zr_{14}$ has been found in the "precatalyst" structure. It should be also noted that in order to fit Pd_2Zr to the experimental XRD pattern, the original lattice parameters of the Pd_2Zr structure (denoted brown in Figure 4), which shows a homogeneity range between 33.3 and 37.0 at % Zr [25], had to be slightly compressed (denoted green in Figure 4). This can be rationalized on the basis of an eventual deviation from the equilibrium structure due to the fast re-cooling of the melt in the preparation process. Most interestingly, and in striking contrast to the observations on Cu-Zr, the respective XRD pattern after catalysis appears essentially unchanged with respect to the bulk phases being present. However, the relative amount of Pd_3Zr increases slightly with respect to Pd_2Zr. This is also understandable on the basis of the Pd-Zr phase diagram: Pd_3Zr is the thermodynamically most stable compound in the Pd-Zr system [25], with the system most likely approaching structural equilibrium. No oxidized bulk ZrO_2 species have also been observed in XRD after MSR, in contrast to Cu-Zr [18]. The stability difference between CuZr and PdZr is,

thus, apparently as follows: PdZr does obviously not experience "deep" bulk corrosion under MSR conditions, in contrast to CuZr, and a thin ZrO_xH_y/Pd^0 surface-near segregation layer is obviously not detectable by XRD. Nevertheless, the related XPS-data in Figure 7 (shown below) clearly show the simultaneous presence of ZrO_xH_y and Pd^0 species at the surface of the intermetallic melt after and (via oxidative segregation of Zr at ambient conditions) already before catalysis.

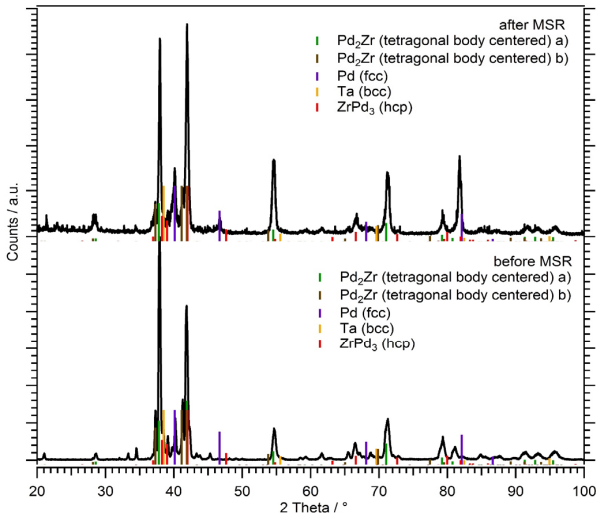

Figure 4. XRD patterns of the Pd-Zr system with a nominal starting stoichiometry of Pd:Zr = 2:1 before (**lower panel**) and after (**upper panel**) methanol steam reforming up to 873 K.

In order to further prove the stability of the bulk-structure and morphology of the Pd-Zr sample, focussed ion beam (FIB)-cut layers have been prepared and accordingly analyzed by TEM and energy-dispersive X-ray analysis (EDX). Figure 5 directly reveals that the Pd-Zr system, despite the presence of metallic Pd and modest amounts of Pd_3Zr in the starting structure, is structurally (left panel of Figure 5) and chemically (middle and right panel of Figure 5) homogeneous over vast regions, especially deep inside the sample bulk. Quantification of the area shown in the panels of Figure 5 reveal an approximate overall stoichiometry of Pd:Zr = 2:1, which is in accordance with the nominal stoichiometry.

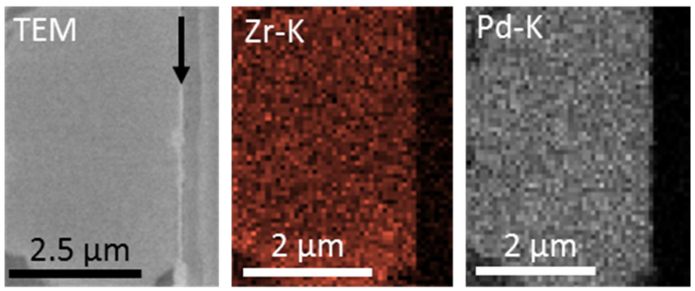

Figure 5. (**Left panel**) TEM image and complementary EDX analyses of a FIB-cut layer of the Pd-Zr system with nominal starting stoichiometry of Pd:Zr = 2:1 before MSR; (**Middle panel**) Zr-K intensity (red); and (**Right panel**) Pd-K intensity (grey). The surface has been denoted by a black arrow. In the right part of the left image, part of the FIB-protecting Pt layer can be seen.

Figure 6 shows that, despite the obvious bulk structural leniency of the system, on the Pd-Zr bulk system, water-activating sites must also be in principal available, as a pronounced CO_2 formation rate is observed. The catalytic light-off temperature of CO_2 and CO at approximately 623 K is very well comparable to that of the inverse Pd/ZrO_xH_y sample (cf. Figure 3), with the CO_2 formation rate

increasing already slightly below 623 K. As on Pd/ZrO_xH_y, low-temperature CO_2 and CO maxima are observed before the maximum formation rate of both CO_2 and CO is approached around 873 K, again very comparable to Pd/ZrO_xH_y. Formation of formaldehyde is also observed, but at a very low rate. Overall, it is worth noting that the catalytic profiles of the inverse Pd/ZrO_xH_y and the intermetallic Pd-Zr sample are qualitatively very well comparable at least with respect to the CO and CO_2 rate maxima.

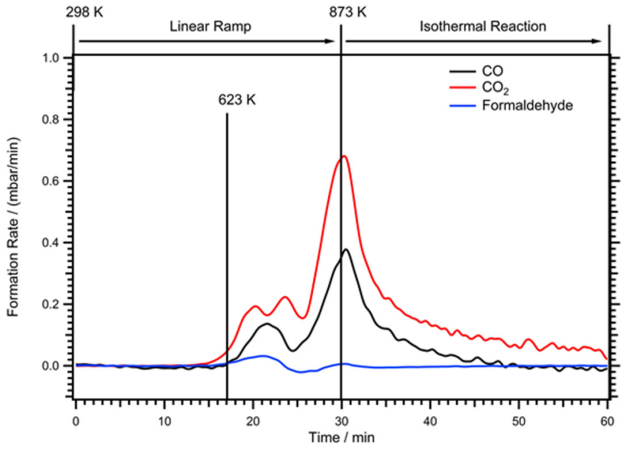

Figure 6. Methanol steam reforming on the Pd-Zr system with nominal starting stoichiometry of Pd:Zr = 2:1. Reaction profile as indicated, reaction conditions: 12 mbar methanol, 24 mbar water, 8 mbar Ar and He added to 1 bar total pressure.

This directly indicates that the hydroxylation behavior must also be similar to a certain extent, a fact that is corroborated by the XP spectra of the Pd-Zr bulk sample before and after MSR (Figure 7). In short, the interpretation of the binding energy shifts and the development of the individual components from the starting structure to that after catalysis is similar to the discussion for Pd/ZrO_xH_y above, with one main difference: the initial Pd-Zr bulk sample, also due to contact to air upon transfer to the batch reactor, is covered by a heavily hydroxylated Zr^{+4} layer (blue dotted line in the Zr 3d doublet). Moreover, this segregated ZrO_xH_y cover layer appears thick enough to fully shield the Zr^0 XPS signal to be expected from the intermetallic bulk. After catalysis, the sample remains clearly hydroxylated, but the Zr 3d components assigned to ZrO_2 become more pronounced, suggesting partial dehydroxylation of Zr^{4+}. Both the Pd 3d and O 1s signals reveal no change before and after catalysis. The C 1 s signal suggests some carbon clean-off reaction.

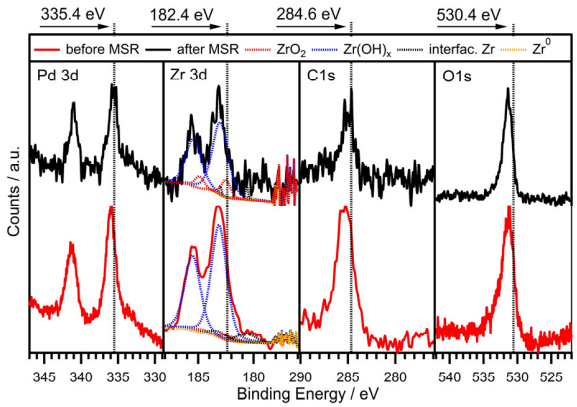

Figure 7. Ex situ XP spectra of the Pd-Zr system with nominal starting stoichiometry of Pd:Zr = 2:1 before and after the MSR reaction up to 873 K (reaction details cf. Figure 6). The Pd 3d, Zr 3d, C 1s and O 1s signals are shown in separate panels.

In summary, the structural and catalytic properties of both Pd-Zr systems are very much alike despite the different preparation approaches: on both systems, water-activating channels are opened via the formation of a Pd/ZrO_xH_y interface, giving rise to CO_2 formation. Due to the selectivity-spoiling effect of metallic Pd, however, the CO_2 selectivity remains low.

2.2. Cu-Zr Bulk Intermetallic Compounds

As already discussed in the introduction, the Cu-ZrO_2 system is a promising catalyst entity for CO_2-selective methanol steam reforming [4]. To further discuss the influence of the Cu:Zr stoichiometry on the catalytic behavior of Cu-Zr bulk phases in methanol steam reforming, we provide a short reprise of previous findings at the beginning, using a nominal Cu:Zr 2:1 stoichiometry [18]. This particular sample, exhibiting an initially (bi)metallic $Cu/Cu_{51}Zr_{14}$ admixture, turned out to be highly active and CO_2 selective in MSR due to selective operando corrosion of Zr and the associated formation of a beneficial co-existence of metallic Cu and oxidized tetragonal ZrO_2. As indicated by the TEM images and the EDX maps, the sample before catalysis is—also deep inside the sample bulk—chemically more or less homogeneous over vast regions (which is comparable to the Pd-Zr compound mixture discussed above) [16]. A particular exception concerns the isolated Cu islands, which almost always, at least in the initial state, are found close to the surface. Catalytic-wise, the sample is extremely CO_2-selective, also after the first catalytic run, with a CO_2 light-off temperature of about 550 K (Figure 8, Panel A). During consecutive runs, the Cu^0–tetragonal ZrO_2 interface self-activates, which is accompanied by a drastic decrease of the CO_2 onset temperature of approximately 80 K to 470 K. Neither CO nor formaldehyde has been observed during the catalytic treatments. Structure and morphology-wise, the activated sample has undergone a significant structural transformation. The surface is now massively enriched in dispersed metallic Cu, with the oxidized Zr acting as a "glue" between the individual Cu particles. In fact, Zr is selectively oxidized both at and below the surface. As this morphology now represents the active and selective state of the catalyst, it is made up by a co-existence of nanoparticulate dispersed metallic Cu and ZrO_2, mostly in its tetragonal modification [18,26]. Figure 9 shows a representative TEM and EDX comparison of the activated state.

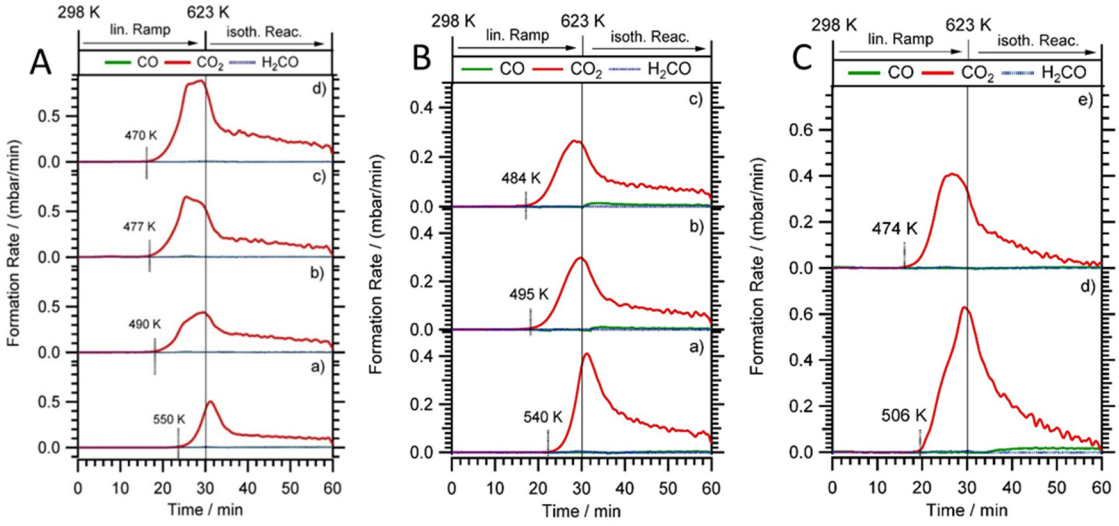

Figure 8. Methanol steam reforming on the initial Cu-Zr metal-intermetallic compound catalysts. (**A**) Cu:Zr stoichiometry = 2:1, (**a**–**d**) four subsequent runs on the same starting material. Note that the decrease of CO_2 formation rate during the isothermal reaction is due to progressive reactant consumption (methanol conversion after 60 min ~100% for (**d**)); (**B**) Catalysis data: (**a**) for run 1; (**b**) for run 2; and (**c**) for run 3 on a Cu/Zr catalyst with the initial ratio Cu:Zr = 9:2; (**C**) (**d**,**e**) runs 1 and 3 for an initial ratio Cu:Zr = 1:2.

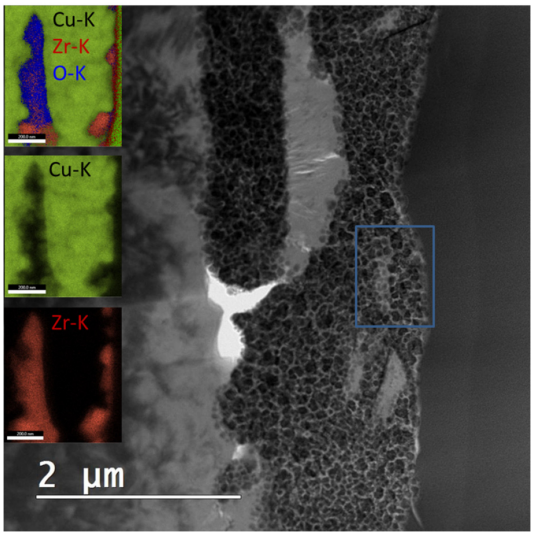

Figure 9. TEM overview image (main panel) and EDX maps (insets) of the *operando*-activated $Cu/Cu_{51}Zr_{14}$ metal-intermetallic compound admixture. To visualize the chemical distribution, the Zr-K, Cu-K and O-K intensities have been used.

X-ray photoelectron spectra in addition showed that Zr^{+4} at the surface is basically partially hydroxylated (i.e., indicating water activation), an obvious prerequisite for CO_2-selective methanol steam reforming [18]. The CO_2 formation rate for the nominal Cu:Zr = 9:2 composition is lower than for an initial nominal composition Cu:Zr of 2:1 (Figure 8, Panel B). The selectivity pattern essentially remains the same. The onset temperature shifts to lower temperatures with every run, as it was also evident for Cu:Zr = 2:1. Panel C highlights the experiments for an initial nominal composition of Cu:Zr = 1:2, which show essentially the same behavior in terms of selectivity, but a slightly lower activity due to the non-optimized stoichiometry in the as-prepared catalyst (i.e., the presence of large amounts of metallic Zr in the initial state). Summarizing the catalytic results of the three different Cu-Zr systems, it is evident that despite the differing nominal starting stoichiometries, the catalytic properties especially in terms of CO_2-selectivity and self-activation are very well comparable. This of course then raises the question, if and to which extent the structure and morphology of the starting structures and the associated hydroxylation degree is also comparable. In principle, due to the different nominal stoichiometries, different starting structures could be expected. The Cu-Zr phase diagram features a variety of stable structures, apart from the thermodynamically most stable $Cu_{51}Zr_{14}$ structure. These include Cu_5Zr, Cu_9Zr_2, Cu_9Zr_3, CuZr and $CuZr_2$ [27,28]. Figures 10 and 11 highlight both the structural analysis based on the XRD patterns of the initial states and their stability and persistence against corrosion in the MSR mixture. For Cu:Zr = 9:2, Figure 10 reveals that the main component before contact to the methanol steam reforming mixture is metallic Cu with $Cu_{51}Zr_{14}$ and Cu_5Zr as additional minor components. After catalysis, metallic Cu is still the dominant component, but modest amounts of $Cu_{51}Zr_{14}$ are also observed. Cu_5Zr has almost entirely decomposed upon contact to the MSR reaction mixture. Most interestingly, no oxidized copper or zirconium species are detected, apart from Ta metal, which served as substrate material for preparation of the intermetallic melt. By catalytic blind experiments using only Ta, influence of the latter was ruled out. This is insofar remarkable, as the catalytic behavior is comparable to that of the Cu:Zr = 2:1 sample, which nevertheless showed metallic Cu and tetragonal ZrO_2 at the surface. Although no oxidized or hydroxylated Zr species could be detected by bulk-sensitive XRD analysis, the respective XP spectra taken before and after the MSR reaction indeed reveal hydroxylated Zr^{4+} species, which might have become segregated as a rather thin layer and/or an (X-ray)-amorphous state in case of the Cu-richest precatalyst (Figure 11, turquoise graph). As observed previously, the Cu intensity increases after catalysis due to the obvious segregation of Cu to the surface of the sample. The Zr 3d intensity decreases accordingly.

The C 1s signal reveals some carbon deposition as a result of the methanol steam reforming reaction. Extending the experiments further to the sample with Zr excess (Figure 11, green traces) indicates no substantial differences in the hydroxylation behavior. All the relevant features are essentially reproduced before and after MSR, which of course is expected on the basis of the already discussed catalytic profiles. The structure of the Cu-Zr sample with strong Zr excess before MSR is essentially characterized by the presence of a body-centered tetragonal $CuZr_2$ phase in co-existence with Zr metal with hcp structure (Figure 12) [29]. In principle, a $CuZr_2$ compound with face-centered cubic structure could be also argued on the basis of the experimental data. After catalysis, Zr metal is absent and the $CuZr_2$ phase has been decomposed in favor of the $Cu_{51}Zr_{14}$ compound. Metallic Cu and XRD-detectable oxidized Zr species are encountered. Part of these species crystallize in the monoclinic ZrO_2 structure, but most of it is present as tetragonal ZrO_2 [30], as observed previously for the Cu:Zr = 2:1 stoichiometry after catalysis. This once again underlines the catalytic importance of the Cu-tetragonal ZrO_2 interface for CO_2-selective methanol steam reforming.

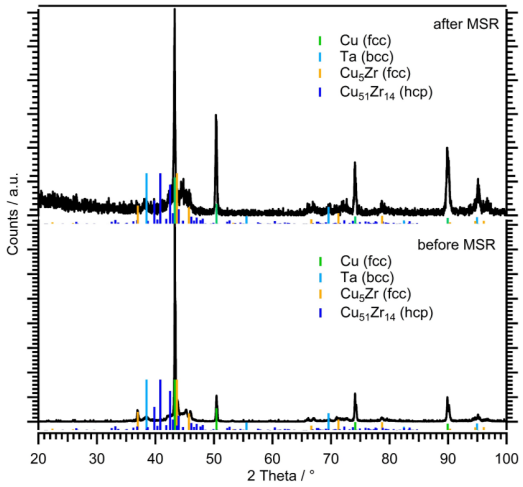

Figure 10. XRD analysis of the Cu-Zr sample with a nominal Cu:Zr = 9:2 stoichiometry: before MSR (**lower panel**); and after MSR (**upper panel**).

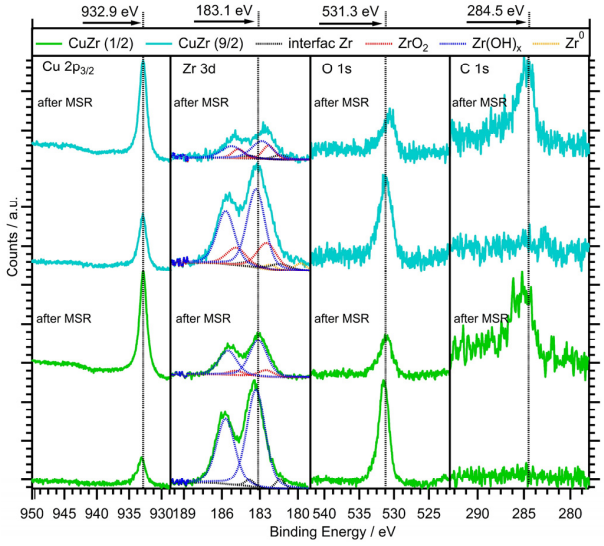

Figure 11. Ex situ collected XP spectra before and after the methanol steam reforming reaction on the Cu-Zr samples with Cu excess (nominal Cu:Zr stoichiometry = 9:2, green traces) and Zr excess (nominal Cu:Zr stoichiometry = 1:2, turquoise traces). The Cu 2p, Zr 3d, O 1s and C 1s signals are shown in separate panels.

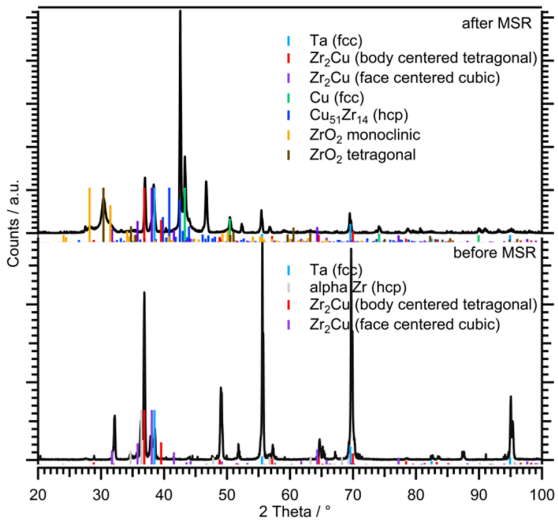

Figure 12. XRD analysis of the Cu-Zr sample with a nominal Cu:Zr = 1:2 stoichiometry: before MSR (**lower panel**); and after MSR (**upper panel**).

3. Materials and Methods

The research was performed using two relevant experimental setups: an UHV-chamber with attached high-pressure recirculating batch reactor and the Innovative Station for In Situ Spectroscopy (Beamline ISISS at the HZB Helmholtz Zentrum Berlin, BESSY II synchrotron).

3.1. UHV Setup

For the former, sample preparation and characterization was performed in a combined preparation/analysis chamber with attached recirculating batch reaction cell operating at ambient pressures, described in more detail elsewhere (base pressure in the low 10^{-9} mbar range) [31]. The sample is heated via e-bombardment, where electrons are ejected from a triple-filament emitter (operated with 30 W heating power) set to −500 V, while the sample is set to +300 V. The electron impact heating power is controlled via the filament emission current. For spectroscopic analysis, the chamber is equipped with a hemispherical electron and ion analyzer (Thermo Fisher Electron Alpha 110), a double anode X-ray gun for XPS (Mg/Al, XR 50, Specs), an ion gun producing 1 kV He^+ ions for ion scattering spectroscopy (ISS; Omicron 100) and an electron beam gun for Auger electron spectroscopy (KPI EGPS-2017B). A mass spectrometer (Balzers) for residual gas analysis and an Ar^+-ion sputter gun for sample cleaning is available. A three way gas inlet allows to dose O_2 (Messer, 5.0), H_2 (Messer 5.0) or O_2-cleaned Ar (Messer 5.0) via leak valves into the main chamber. All XP spectra are collected using non-monochromatized Mg Kα radiation ($h\nu$ = 1253.6 eV) at 250 W and at the magic angle to the analyzer. For XPS, the analyzer is operated at a constant pass energy of 20 eV.

3.2. Preparation of Materials

To prepare the inverse Pd-Zr model systems, zirconium (IV) *tert*-butoxide Zr(O-*t*-C_4H_9)$_4$ (Sigma-Aldrich, purity: 99,999%) is used as ALD/CVD precursor. Prior to dosing ZTB, several cycles of freeze-and-thaw are performed (cooling temperature: 77 K, freezing point ZTB: 269 K). ZTB has a sufficient vapor pressure at room temperature to dose it directly through a leak-valve. Before sample exposure, the preparation chamber is exposed to the precursor at 5×10^{-7} mbar for 5 min to passivate the chamber walls against precursor decomposition. The exposure is calculated from uncorrected ion gauge measurements in Langmuir, involving exposure pressures in the range of 5×10^{-8} to 5×10^{-6} mbar. The adsorbate coverage is determined from XP models as outlined in Ref. [32–35]. In order to validate the CVD-based catalytic results and to obtain a broader experimental basis of the Pd-Zr^0 system with respect to methanol steam reforming performance, also an intermetallic bulk

phase of Pd and Zr^0 was prepared. Synthesis was carried out under HV conditions (base pressure 1×10^{-7} mbar) by heating stacked small pieces of the above-specified pure Pd and Zr foil samples (Alfa Aesar, purity: 99.95%, thickness: 0.127 mm) resistively in a Ta crucible in the nominal atomic ratio 2:1. At a temperature slightly above the melting point of Pd (1828 K), spontaneous reaction between Pd and Zr leads to an intermetallic Pd-Zr melt, which then re-crystallizes toward Pd-Zr bulk phases during re-cooling in vacuum. Subsequently, the sample is transferred to the UHV system with attached batch reactor for analysis and catalytic testing. The nominal 2:1 Pd:Zr stoichiometry (i.e., with Pd excess) is chosen with the idea to maintain at least some active Pd metal surface co-existing with oxidatively segregated Zr species under reaction conditions. Moreover, an excess of Pd is necessary because the melting point of Zr is very high and complete intermetallic formation reaction of Pd with Zr is necessary in order to distribute the Zr^0 homogeneously in the melt. Preparation of the corresponding Cu-Zr intermetallic catalyst pre-cursor was carried out under comparable experimental conditions by using Cu foil (Goodfellow, purity: 99.95%, thickness: 0.125 mm) and Zr foil, as specified above. The sample holder boat is then heated resistively under similar high vacuum conditions slightly above the melting temperature of Cu (1360 K), but again far below the melting temperature of Zr (2130 K). At this temperature, solid Zr reacts with the molten Cu to form a uniform melt, whereas at the same time the evaporation of Cu is negligibly low. These preparation cycles have been repeated for the three nominal Cu:Zr atomic ratios of 9:2, 2:1 and 1:2. Due to the different nominal starting stoichiometries, XRD analyses reveal different initial Cu-Zr intermetallic structures in admixtures with metallic Cu (cf. Figures 10 and 11 and Ref. [18]).

3.3. Catalytic Measurements

All catalytic experiments for the inverse Pd-Zr sample are performed using a 20×18 mm^2 ultra-clean polycrystalline Pd foil (Goodfellow, 99.95%) with a thickness of 0.125 mm (for reference experiments on pure ZrO_2, a pre-oxidized 0.127 mm Zr foil with the same size (Alfa Aesar, purity: 99.95%) is used). The foils are cleaned before loading to the UHV chamber in a water and an ethanol ultrasonic bath for 20 min, respectively. For catalytic testing in the ambient-pressure re-circulating batch reaction cell, the all-quartz-glass high-pressure (up to 1 bar) batch reactor (accessible via a long z-transfer rod allowing fast and reliable transfer without exposure to air) is equipped with a gas chromatograph providing either intermediate or continuous MS detection to determine the exact gas composition at any point of reaction. Continuous partial pressure detection is performed via a direct capillary leak to the EID of the GC-MS. The quartz-glass reactor with a total circulation volume of 296 mL is designed to measure small reaction rates and selectivity patterns within a temperature range between room temperature and 1300 K. A circulation pump ensures a constant flow and gas intermixing and an attached gas-premixing unit allows to set arbitrary compositions of the attached reactant vapors or introduced gases (methanol, methane (5.0), deionized and degassed water, CO_2 (5.0), O_2 (5.0), H_2 (5.0), Ar (5.0) and He (5.0)). The sample holder itself is entirely made of quartz glass to avoid background reactivity from hot metal parts and is designed for 20 mm $\times$ 18 mm metal foils. A partial pressure of 8–30 mbar argon added to all gas mixtures allows accounting for the pressure-change due to the temperature program and the simultaneous gas loss through the capillary leak for continuous EID-MS detection. For partial pressure calculations, all base-line-corrected MS signals are calibrated using pure substances with quantitative consideration of fragmentation. For all MSR catalytic experiments shown in this work, an excess of water has been used to avoid eventual methanol dehydrogenation due to water shortage in the reaction mixture. In all experiments, He is added to a total pressure of 1 bar, in order to optimize both heat transfer and gas intermixing via efficient recirculation. After an equilibration and premixing period of 10 min, a heating routine (rate 10 $K \cdot min^{-1}$) up to 673 K is performed, followed by an isothermal period at 673 K, respectively 873 K (rate 19 $K \cdot min^{-1}$) followed by an isothermal period at 873 K. Exact experimental conditions are given in the respective Figure captions. For discussion about mass and heat transport limitations, we refer to a thorough discussion of the catalytic setup in Ref. [31].

3.4. Structural Characterization

Elemental and structural analysis was performed by electron microscopy and EDX spectroscopy. The transmission electron microscopic (TEM) investigations were performed using a FEI TECNAI F20 field emission TEM, equipped with a high angle annular dark field STEM detector (HAADF), an Apollo XLTW SDD X-Ray detector and a GATAN GIF Tridiem image filter. The spatial resolution of the EDX maps is about 1 nm. The TEM samples were prepared by means of focused ion beam (FIB) using a FEI Quanta 200 dual beam FIB and gentle Ar^+-ion polishing in order to remove beam damage from prior FIB milling. To protect the surface, a Pt covering layer is deposited prior to the FIB process. Further, the layer is cut by using a Ga ionic beam, whose energy is decreased to about 1 kV in the last preparation step. This avoids damage to the cut layer.

X-ray powder diffraction data were collected at ambient conditions with a Bruker AXS D8-Advance powder diffractometer using $CuK_{\alpha 1}$ and $CuK_{\alpha 2}$ radiation (λ_1 = 1.5406 Å; λ_2 = 1.5444 Å; 40 kV; 40 mA). The diffractometer exhibits a Bragg-Brentano reflection geometry with θ-θ coupling and parallel beam optics. An energy-dispersive Si(Li) semiconducting Sol-X detector was used. Data acquisition was performed in the 2θ range between 10° and 110° with a step width of 0.02° and a counting time of 5 s.

3.5. In Situ XPS Setup

Synchrotron-based in situ XPS experiments were performed at the ISISS (Innovative Station for in situ Spectroscopy) beamline at the HZB/BESSY II synchrotron in Berlin, Germany. The experimental apparatus consists of a load lock and an in situ cell connected to the XPS spectrometer via differential pumping stages. The experimental apparatus has been described in the literature in detail previously [36]. Samples are heated in the in situ cell via a near-infrared semiconductor laser (λ = 808 nm) from the rear. The temperature is measured by a *K*-type (chromel−alumel) thermocouple positioned between sample holder back plate and Pd foil. All in situ experiments are performed on the same Pd foil sample that is used for the model catalyst preparation in the UHV instrument with attached batch reactor. For the inverse Pd-Zr sample, the same ZTB cylinder/leak valve setup discussed above is transferred to ISISS beamline. Due to the fact that ZTB only interacts with surfaces hotter than 500 K, it is safe to dose the organometallic precursor into the analysis chamber without any Zr deposition on the components of the vacuum system or on the X-ray window. The growth of ZTB can then be followed directly via XPS. To determine a potential influence of the X-ray beam on the sample structure and chemistry, heating was performed at random checking with and without X-ray beam. As no distinct changes in the spectra between the two runs have been observed, this influence is considered to be marginal. Monochromator control allows to choose photon energies corresponding to kinetic energies of the ejected photoelectrons of 120 eV for all monitored core-level photoemission peaks in order to extract information from a constant information depth and to yield the same attenuation of the photoelectrons through the gas phase. Due to the fact that 95% of the signal arises from a sample depth up to ~1 nm, this operation mode is considered to be maximum "surface sensitive". Photoelectrons are collected in the direction normal to the surface at constant pass energy of 10 eV. Binding energies were referenced to the Fermi edge, which is measured each time the monochromator moves to a new position, i.e., whenever the incident photon energy was changed. Photoemission peak intensities are corrected for the respective photon flux at a given photon energy. The BESSY II synchrotron operates in top-up mode (constant ring current); hence, no additional correction for the ring current was required. Since all photoemission peaks were collected at the same kinetic energy of photoelectrons (120 eV), the attenuation through the gas phase was the same for all-core levels and, thus, cancels out in coverage calculations.

3.6. Analysis of the XPS Data

All spectra are analyzed using the CasaXPS software program, version 2.3.16 Pre-rel 1.4 (Casa Software Ltd. [37]. A Shirley background is applied to all spectra and the associated Scofield relative sensitivity factors are used for quantification. For peak fitting of the Zr 3d peaks, a weighted sum of Gaussian and Lorenzian peak shapes (CasaXPS line shape SGL(30)) is assumed, using a doublet separation (Zr $3d_{5/2}$ vs. Zr $3d_{3/2}$) of 2.4 eV for both metallic Zr [38] and zirconia [39] for fitting. The doublet area is kept constant at 3:2 as arising from spin-orbit d-electron coupling. Electron attenuation lengths were taken from the NIST database SR 82 [40] and the orbital asymmetric parameter from the ELETTRA online database of Ref. [41]. The quantification of the XPS data is given as atomic percentages or coverage/thickness. The atomic percentage is estimated assuming homogeneously mixed elements. Since an adlayer on the substrate surface is not a homogeneous system, the coverage/thickness gives a better representation. The ZrO_xH_y surface coverage is calculated assuming a non-attenuating adlayer on a semi-infinite substrate [20,23–25]. As the maximum ZrO_xH_y layer thicknesses remained in the sub-monolayer regime in this study, the influence of a potential attenuation effect of the photoelectrons by the overlayer remains negligible even for the highest exposures. This is tested by comparing the results on a ~1 ML ZrO_xH_y covered sample, using both an attenuating and non-attenuating overlayer model, which eventually shows negligible differences. Details of these calculations are given in Ref. [32–35]

4. Conclusions

We have shown for both the Pd-Zr and the Cu-Zr systems, that the interaction between Pd/Cu and Zr can in principle give rise to a synergistically operating catalytic entity providing water activating channels that are basically absent on the noble metal part of the catalytic sample. For Pd-Zr, as previously documented for Cu-Zr, different preparation approaches (using an inverse model system and a bulk sample) lead to very similar materials with respect to structure, hydroxylation degree and catalytic behavior. Furthermore, the experiments on Cu-Zr strongly indicate that independent of the initial structure and composition (ranging from Cu_5Zr over $Cu_{51}Zr_{14}$ to $CuZr_2$ in admixtures with metallic Cu or Zr), the catalytically active and CO_2-selective metal-oxide interface resulting from operando corrosive decomposition of the intermetallic compounds is very similar. Hence, the catalysts are capable of self-adjustment in the methanol steam reforming mixture, essentially yielding "supported" Cu/ZrO_xH_y entities with superior catalytic behavior.

Acknowledgments: The work was performed within the platform "Material- and Nanoscience" at the University of Innsbruck. Financial support of the SFB project FOXSI F4503 and F4501, funded by the Austrian Science Fund, is greatly acknowledged. We thank HZB/BESSY I for support under proposal 14201485-ST.

Author Contributions: N.K. and L.M. performed the catalytic tests and the XP spectroscopy. D.S. and N.K. recorded and analyzed the XRD data. J.B. performed the TEM and EDX experiments; A.K.-G. and M.H. carried out the in situ XP spectroscopy. B.K. designed and analyzed the in situ XPS experiments and data. S.P. wrote the manuscript.

Conflicts of Interest: The authors declare no conflict of interest. The founding sponsors had no role in the design of the study; in the collection, analyses, or interpretation of data; in the writing of the manuscript, and in the decision to publish the results.

References

1. Fujimoto, K.-I.; Ribeiro, F.H.; Avalos-Borja, M.; Iglesia, E. Structure and Reactivity of PdO_x/ZrO_2 Catalysts for Methane Oxidation at Low Temperatures. *J. Catal.* **1998**, *179*, 431–442. [CrossRef]
2. Liu, S.H.; Chuah, G.K.; Jaenicke, S. Liquid-phase Oppenauer Oxidation of Primary Allylic and Benzylic Alcohols to Corresponding Aldehydes by Solid Zirconia Catalysts. *J. Mol. Catal. A Chem.* **2004**, *220*, 267–274. [CrossRef]
3. He, D.; Ding, Y.; Luo, H.; Li, C. Effects of Zirconia Phase on the Synthesis of Higher Alcohols over Zirconia and Modified Zirconia. *J. Mol. Catal. A Chem.* **2004**, *208*, 267–271. [CrossRef]

4. Behrens, M.; Armbrüster, M. Methanol Steam Reforming. In *Catalysis for Alternative Energy Generation*; Guczi, L., Erdôhelyi, A., Eds.; Springer: New York, NY, USA, 2012; pp. 175–235.
5. Sudarsanam, P.; Mallesham, B.; Reddy, P.; Großmann, S.; Grünert, D.; Reddy, B.M. Nano-Au/CeO_2 Catalysts for CO Oxidation: Influence of Dopants (Fe, La and Zr) on the Physicochemical Properties and Catalytic Activity. *Appl. Catal. B Environ.* **2014**, *144*, 900–908. [CrossRef]
6. Du, W.; Zhao, G.; Chang, H.; Shi, F.; Zhu, Z.; Qian, X. Photocatalytic Studies of Ho-Zr-O Nano-Composite with Controllable Composition and Defects. *Mater. Charact.* **2013**, *83*, 178–186. [CrossRef]
7. Behrens, M.; Brennecke, D.; Girgsdies, F.; Kißner, S.; Trunschke, A.; Nasrudin, N.; Zakaria, S.; Fadilah Idris, N.; Abd Hamid, S.B.; Kniep, B.; et al. Understanding the Complexity of a Catalyst Synthesis: Co-Precipitation of Mixed Cu, Zn, Al Hydroxycarbonate Precursors for Cu/ZnO/Al_2O_3 Catalysts Investigated by Titration Experiments. *Appl. Catal. A Gen.* **2011**, *392*, 93–102. [CrossRef]
8. Velu, S.; Suzuki, S.; Gopinath, K.; Yoshida, C.S.; Hattori, H. XPS, XANES and EXAFS Investigations of CuO/ZnO/Al_2O_3/ZrO_2 Mixed Oxide Catalysts. *Phys. Chem. Chem. Phys.* **2002**, *4*, 1990–1999. [CrossRef]
9. Purnama, H.; Girgsdies, F.; Ressler, T.; Schattka, J.H.; Caruso, R.A.; Schomacker, R.; Schlögl, R. Activity and Selectivity of a Nanostructured CuO/ZrO_2 Catalyst in the Steam Reforming of Methanol. *Catal. Lett.* **2004**, *94*, 61–68. [CrossRef]
10. Purnama, H.; Ressler, T.; Jentoft, R.E.; Soerijanto, H.; Schlögl, R.; Schomäcker, R. CO Formation/Selectivity for Steam Reforming of Methanol with a Commercial CuO/ZnO/Al_2O_3 catalyst. *Appl. Catal. A Gen.* **2004**, *259*, 83–94. [CrossRef]
11. Velu, S.; Suzuki, K.; Kapoor, M.P.; Ohashi, F.; Osaki, T. Selective Production of Hydrogen for Fuel Cells via Oxidative Steam Reforming of Methanol over CuZnAl(Zr)-oxide Catalysts. *Appl. Catal. A Gen.* **2001**, *213*, 47–63. [CrossRef]
12. Wu, G.-S.; Mao, D.-S.; Lu, G.-Z.; Cao, Y.; Fan, K.-N. The Role of the Promoters in Cu Based Catalysts for Methanol Steam Reforming. *Catal. Lett.* **2009**, *130*, 177–184. [CrossRef]
13. Breen, J.P.; Ross, J.R. Methanol Reforming for Fuel-Cell Applications: Development of Zr-Containing Cu-Zn-Al Catalysts. *Catal. Today* **1999**, *51*, 521–533. [CrossRef]
14. Mayr, L.; Klötzer, B.; Zemlyanov, D.; Penner, S. Steering of Methanol Reforming Selectivity by Zirconia–Copper Interaction. *J. Catal.* **2015**, *321*, 123–132. [CrossRef]
15. Mayr, L.; Shi, X.; Köpfle, N.; Klötzer, B.; Zemlyanov, D.; Penner, S. Tuning of the Copper-Zirconia Phase Boundary for Selectivity Control of Methanol Conversion. *J. Catal.* **2016**, *339*, 111–122. [CrossRef]
16. Mayr, L.; Shi, X.; Köpfle, N.; Klötzer, B.; Schmidmair, D.; Bernardi, J.; Schwarz, S.; Penner, S. Boosting Hydrogen Production from Methanol/Water by In Situ Activating Bimetallic Cu-Zr. *ChemCatChem* **2016**, *8*, 1778–1781. [CrossRef]
17. Palo, D.R.; Dagle, R.A.; Holladay, J.D. Methanol steam reforming for hydrogen production. *Chem. Rev.* **2007**, *107*, 3992–4021. [CrossRef] [PubMed]
18. Rameshan, C.; Stadlmayr, W.; Weilach, C.; Penner, S.; Lorenz, H.; Hävecker, M.; Blume, R.; Rocha, T.; Teschner, D.; Knop-Gericke, A.; et al. Subsurface-Controlled CO_2 Selectivity of PdZn Near-Surface Alloys in H_2 Generation by Methanol Steam Reforming. *Angew. Chem. Int. Ed.* **2010**, *49*, 3224–3227. [CrossRef] [PubMed]
19. Rameshan, C.; Stadlmayr, W.; Penner, S.; Lorenz, H.; Memmel, N.; Hävecker, M.; Blume, R.; Teschner, D.; Rocha, T.; Zemlyanov, D.; et al. Hydrogen Production by Methanol Steam Reforming on Copper Boosted by Zinc-Assisted Water Activation. *Angew. Chem. Int. Ed.* **2012**, *124*, 3057–3061. [CrossRef]
20. Mayr, L.; Shi, X.-R.; Köpfle, N.; Milligan, C.; Zemlyanov, D.; Knop-Gericke, A.; Hävecker, M.; Klötzer, B.; Penner, S. Chemical vapor deposition-prepared sub-nanometer Zr clusters on Pd surfaces: Promotion of methane dry reforming. *Phys. Chem. Chem. Phys.* **2016**, *18*, 31586–31599. [CrossRef] [PubMed]
21. Lim, K.H.; Chen, Z.X.; Neyman, K.M.; Rösch, N. Comparative Theoretical Study of Formaldehyde Decomposition on PdZn, Cu, and Pd Surfaces. *J. Phys. Chem. B* **2006**, *110*, 14890–14897. [CrossRef] [PubMed]
22. Yazyev, O.V.; Louie, S.G. Electron Transport in Polycrystalline Graphene. *Nat. Mater.* **2010**, *9*, 806–809. [CrossRef] [PubMed]
23. Schubert, K.; Bhan, S.; Burkhardt, W.; Gohle, R.; Meissner, H.G.; Poetzschke, M.; Stolz, E. Einige strukturelle Ergebnisse an metallischen Phasen (5). *Naturwissenschaften* **1960**, *47*, 303. [CrossRef]

24. Harris, I.E.; Norman, M. Observations on the lattice spacings of some αPd-X solid solutions and some Pd_3X phases. *J. Less Common Met.* **1970**, *22*, 127–133. [CrossRef]
25. Hu, J.Q.; Xie, M.; Pan, Y.; Yang, Y.C.; Liu, M.M.; Zhang, J.M. The electronic, elastic and structural properties of Pd-Zr intermetallic. *Comput. Mater. Sci.* **2012**, *51*, 1–6. [CrossRef]
26. Mayr, L.; Köpfle, N.; Klötzer, B.; Götsch, T.; Bernardi, J.; Schwarz, S.; Keilhauer, T.; Armbrüster, M.; Penner, S. Microstructural and Chemical Evolution and Analysis of a Self-Activating CO_2-Selective Cu-Zr Bimetallic Methanol Steam Reforming Catalyst. *J. Phys. Chem. C* **2016**, *120*, 25395–25404. [CrossRef]
27. Okamoto, H. Cu-Zr (Copper-Zirconium) Phase Diagram, H. *J. Phase Equilib. Diffus.* **2008**, *29*, 204. [CrossRef]
28. Forey, P.; Glimois, J.L.; Feron, J.L.; Develey, G.; Becle, C.C.R. Synthesis, Characterization and Crystal Structure of Cu_5Zr. *Seances Acad. Sci. Ser. C* **1980**, *291*, 177–181.
29. Ahlyen, P.J.; Andersson, Y.; Rundqvist, S.; Tellgren, R. A neutron diffraction study of Zr_3PD_{3-x}. *J. Less Common Met.* **1990**, *161*, 269–278. [CrossRef]
30. Bouvier, P.; Djurado, E.; Ritter, C.; Dianoux, A.J.; Lucazeau, G. Low temperature phase transformation of nanocrystalline tetragonal ZrO_2 by neutron and Raman scattering studies. *Int. J. Inorg. Mater.* **2001**, *3*, 647–654. [CrossRef]
31. Mayr, L.; Rameshan, R.; Klötzer, B.; Penner, S.; Rameshan, C. Combined UHV/High-Pressure Catalysis Setup for Depth-Resolved Near-Surface Spectroscopic Characterization and Catalytic Testing of Model Catalysts. *Rev. Sci. Instrum.* **2014**, *85*, 055104. [CrossRef]
32. Gharachorlou, A.; Detwiler, M.D.; Gu, X.K.; Mayr, L.; Klötzer, B.; Greeley, J.; Reifenberger, R.G.; Delgass, W.N.; Ribeiro, F.H.; Zemlyanov, D.Y. Trimethylaluminum and Oxygen Atomic Layer Deposition on Hydroxyl-Free Cu(111). *ACS Appl. Mater. Interfaces* **2015**, *7*, 16428–16439. [CrossRef] [PubMed]
33. Gharachorlou, A.; Detwiler, M.D.; Mayr, L.; Gu, X.K.; Greeley, J.; Reifenberger, R.G.; Delgass, W.N.; Ribeiro, F.H.; Zemlyanov, D.Y. Surface Chemistry of Trimethylaluminum on Pd(111) and Pt(111). *J. Phys. Chem. C* **2015**, *119*, 19059–19072. [CrossRef]
34. Gharachorlou, A.; Detwiler, M.D.; Nartova, A.V.; Lei, Y.; Lu, J.; Elam, J.W.; Delgass, W.N.; Ribeiro, F.H.; Zemlyanov, D.Y. Palladium Nanoparticle Formation on TiO_2(110) by Thermal Decomposition of Palladium(II) Hexafluoroacetylacetonate. *ACS Appl. Mater. Interfaces* **2014**, *6*, 14702–14711. [CrossRef] [PubMed]
35. Paul, R.; Reifenberger, R.G.; Fisher, T.S.; Zemlyanov, D.Y. Atomic Layer Deposition of FeO on Pt(111) by Ferrocene Adsorption and Oxidation. *Chem. Mater.* **2015**, *27*, 5915–5924. [CrossRef]
36. Knop-Gericke, A.; Kleimenov, E.V.; Hävecker, M.; Blume, R.; Teschner, D.; Zafeiratos, S.; Schlögl, R. X-ray Photoelectron Spectroscopy for Investigation of Heterogeneous Catalytic Processes. *Adv. Catal.* **2009**, *52*, 213–272.
37. *CasaXPS Version 2.3.16 Pre-rel 1.4*; Casa Software Ltd.: Devon, UK, 2011.
38. Wagner, C.D.; Riggs, W.M.; Davis, L.E.; Moulder, J.F.; Muilenberg, G.E. *Handbook of X-ray Photoelectron Spectroscopy*; Perkin-Elmer Corporation, Physical Electronics Division: Eden Prairie, MN, USA, 1979; Volume 55344.
39. Majumdar, D.; Chatterjee, D. X-ray Photoelectron Spectroscopic Studies on Yttria, Zirconia, and Yttria-Stabilized Zirconia. *J. Appl. Phys.* **1991**, *70*, 988–992. [CrossRef]
40. Powell, C.J.; Jablonski, A. *NIST Electron Effective-Attenuation-Length Database SRD 82*, version 1.3; National Instititue of Standards and Technology: Gaithersburg, MD, USA, 2011.
41. Yeh, J.J. *Atomic Calculation of Photoionization Cross-Sections and Asymmetry Parameters*; Gordon and Breach Science Publishers: Langhorne, PE, USA, 1993.